Lawrence Berkeley National Laboratory
Recent Work

Title
Enhancing the Performance of a Fused-Ring Electron Acceptor by Unidirectional Extension.

Authors
Jia, Boyu
Wang, Jing
Wu, Yao
et al.

Enhancing the Performance of a Fused-Ring Electron Acceptor by Unidirectional Extension

Boyu Jia,[†] Jing Wang,[‡] Yao Wu,[§] Mingyu Zhang,[†] Yufeng Jiang,[∥] Zheng Tang,[‡] Thomas P. Russell,[§,∥] and Xiaowei Zhan*,[†]

[†]Department of Materials Science and Engineering, College of Engineering, Key Laboratory of Polymer Chemistry and Physics of Ministry of Education, Peking University, Beijing 100871, China

[‡]Center for Advanced Low-Dimension Materials, State Key Laboratory for Modification of Chemical Fibers and Polymer Materials, College of Materials Science and Engineering, Donghua University, Shanghai 201620, China

[§]Department of Polymer Science and Engineering, University of Massachusetts∂Amherst, 120 Governors Drive, Amherst, Massachusetts 01003, United States

[∥]Materials Sciences Division, Lawrence Berkeley National Laboratory, 1 Cyclotron Road, Berkeley, California 94720, United States

ABSTRACT: The unidirectional extension of a smaller fused-ring system into a larger one in a single direction will increase the conjugation length, allowing a fine-tuning of electronic properties. Here, we designed and synthesized a unidirectionally extended fused-8-ring-based nonfullerene acceptor, AOIC, and a bidirectionally extended fused-11-ring electron acceptor, IUIC2, and compared these with the parent fused-5-ring electron acceptor, F5IC. They share the same electron-accepting groups and alkylphenyl side chains but have different fused-ring electron-donating units. Core extension from 5 to 11 rings up-shifts the energy levels, red shifts the absorption spectra, and reduces bandgaps. The unidirectionally extended AOIC has the highest mobility (2.1×10^{-3} cm^2 V^{-1} s^{-1}) relative to the parent F5IC (1.0×10^{-3} cm^2 V^{-1} s^{-1}) and the bidirectionally extended IUIC2 (4.7×10^{-4} cm^2 V^{-1} s^{-1}). Upon blending with the donor PTB7-Th, AOIC-based organic photovoltaic cells show an efficiency of 13.7%, much better than that of F5IC-based cells (5.61%) and IUIC2-based cells (4.48%).
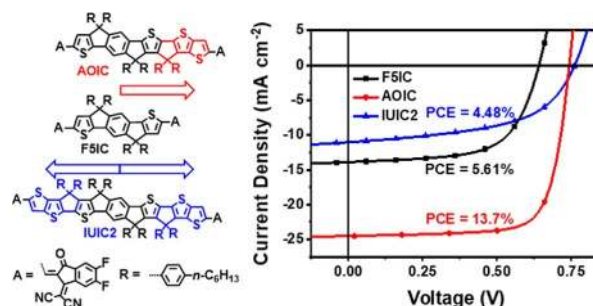
INTRODUCTION

Organic solar cells (OSCs) present some attractive merits, such as being lightweight, transparent, and flexible, and have received extensive attention in the last two decades.[1−4] Fullerenes and their derivatives have been the "workhorse" electron acceptors in OSCs, but the limited variability of energy levels, poor absorption in the visible region, and the instability of the morphology[5,6] have limited the efficiencies achievable. Nonfullerene acceptors, on the other hand, have opened a wealth of opportunities thanks to new chemistries that have led to devices with exceptional efficiencies and have received increasing attention over the past several years.[7−17] Since Zhan and co-workers pioneered fused-ring electron acceptors (FREAs) with the synthesis of landmark molecule ITIC in 2015,[18] nonfullerene-based OSCs have continually broken power conversion efficiency (PCE) records, which increased from <7% to >16% for single-junction cells[19−26] and even up to >17% for tandem cells.[27] FREAs consist of a rigid aromatic fused-ring core substituted with aryl and/or alkyl side chains, coupled with two strong electron-accepting groups.[28−51] For the electron-donating fused-ring cores, most efforts have focused on modifying the indacenodithiophene

(IDT) unit, for example, replacing the central phenyl ring with naphthalene[30] or a thienothiophene ring[31] or replacing peripheral thiophene units with fused thiophene units.[52,53] Most IDT-based larger fused-ring cores are synthesized by extending IDT from both sides,[54,55] which restricts the precise tuning of energy levels, absorption, and the molecular packing of the molecules.

Here we demonstrate a unidirectional extension strategy to synthesize larger fused-ring cores. Unidirectional extension is the extension of a smaller fused-ring system into a larger fused- ring system in only one direction. The unidirectional extension increases the conjugation length in a smaller stepwise manner relative to the bidirectional extension, allowing a fine-tuning of the electronic properties of the molecules. Moreover, the unidirectional extension may generate an asymmetric molec- ular structure that can increase the molecular dipole moment and dielectric constant, thereby reducing the exciton binding energy.[56] Furthermore, the bidirectional extension usually requires a Stille coupling reaction involving toxic organotin

reagents. Consequently, we designed and synthesized a new fused-octacyclic building block by the unidirectional extension of IDT with a single diarylcyclopentadienylthieno[3,2-*b*]- thiophene, with which a new FREA, AOIC, was synthesized (Scheme 1). We also designed and synthesized a new fused-

Scheme 1. Chemical Structures of F5IC, AOIC, IUIC2, and PTB7-Th
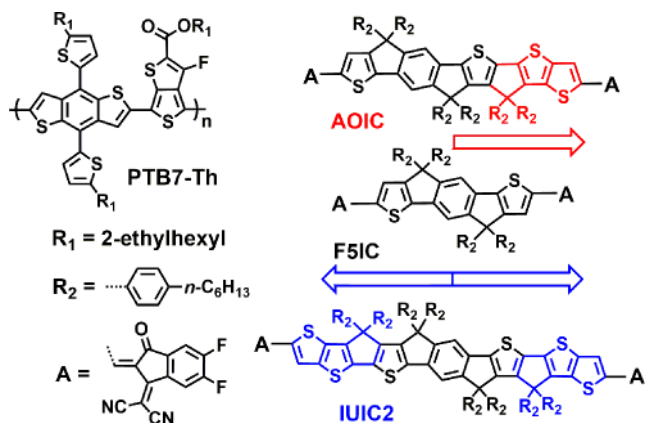
undecacyclic building block by a bidirectional extension of IDT with double diarylcyclopentadienylthieno[3,2-*b*]- thiophenes, with which another new FREA, IUIC2, was synthesized (Scheme 1). We compare AOIC and IUIC2 with the IDT parent FREA, F5IC, reported in our previous work.[52] These three compounds have cores of different sizes but the same end groups, 3-(1,1-dicyanomethylene)-5,6-difluoro-1- indanone (2FIC).[36] From F5IC to AOIC and IUIC2, the core size increases from a fused-5-ring to a fused-11-ring

system, the energy levels shift up, the absorption spectra red shift, and the band gaps decrease. The OSCs based on AOIC blended with a classical polymer donor PTB7-Th[57] have a PCE of 13.7%, much better than that of the F5IC- (5.61%) and IUIC2-based devices (4.48%) and among the highest values for PTB7-Th-based OSCs.

RESULTS AND DISCUSSION

Synthesis and Characterization. AOIC and IUIC2 were synthesized as shown in Scheme 2 and fully characterized (Supporting Information). Here, we carried out the nontoxic Negishi coupling reaction to synthesize unidirectional and bidirectional extended fused-ring cores (AO and IU2), as opposed to the often-used Stille cross coupling with toxic organotin reagents. The Pd-catalyzed Negishi coupling reaction of ethyl 2-bromothieno[3,2-*b*]thiophene-3-carboxy- late (TT-AB, 1.0 equiv) with IDT-ZnCl, which was generated through the reaction of an IDT single lithium reagent with $ZnCl_2$, afforded the new intermediate IDT-1TT. Bidirection- ally extended counterpart IDT-2TT was synthesized through the same reaction of TT-AB (2.5 equiv) with IDT-2ZnCl, which was generated through the reaction of an IDT double lithium reagent with $ZnCl_2$. Reaction between IDT-1TT/IDT- 2TT and Grignard reagent 4-hexylphenyl-1-magnesium bro- mide followed by intramolecular annulation via acid-mediated Friedel−Crafts reaction afforded AO/IU2. The formylation of AO/IU2 through lithiation and then quenching with dimethyl-formamide (DMF) yielded aldehyde AO-CHO/IU2-CHO. Knoevenagel condensation between AO-CHO/IU2-CHO and 2FIC yielded AOIC/IUIC2. Overall yields of AOIC and IUIC2 were 26.7 and 15.3%, respectively. AOIC and IUIC2 exhibit good thermal stability with decomposition temper-
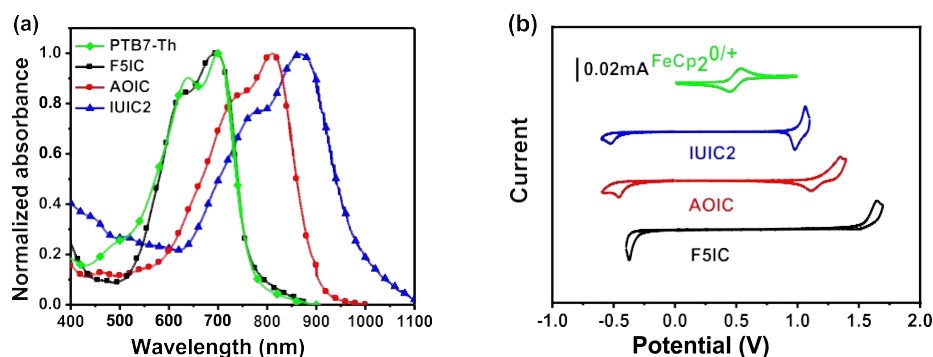
Scheme 2. Synthesis Routes of AOIC and IUIC2

R = ⟨ ⟩—n-C₆H₁₃
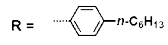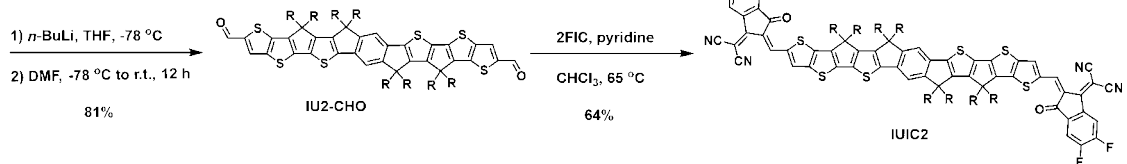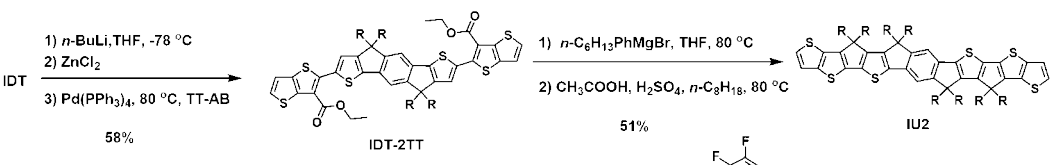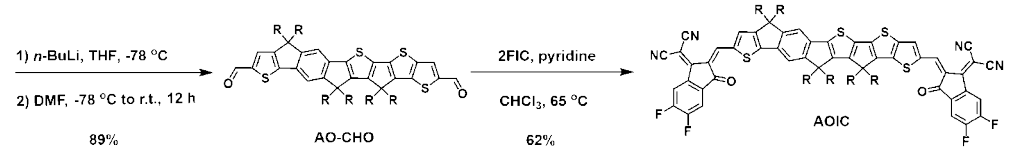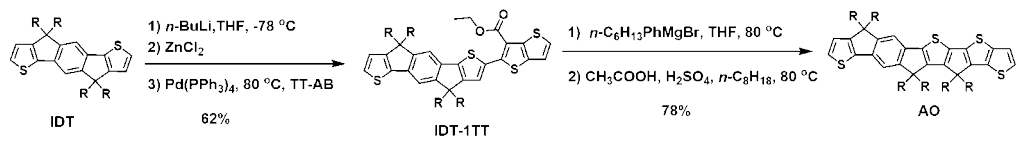
Figure 1. (a) Absorption spectra of F5IC, AOIC, and IUIC2 in thin films. (b) Cyclic voltammograms for F5IC, AOIC, and IUIC2 in CH_3CN/0.1 M $[Bu_4N]^+[PF_6]^-$ at 100 mV s^{-1}, in which the horizontal scale refers to an Ag/AgCl electrode as a reference electrode.

Table 1. Basic Properties of F5IC, AOIC, and IUIC2

compound	T_d (°C)	λ_{max} (nm)		E_g (eV)	ε (M^{-1} cm^{-1})	HOMO (eV)	LUMO (eV)	
		solution	film					
F5IC	344	666	694	1.64	2.0×10^5	−5.82	−4.05	9.6 ± 0.8 (10)
AOIC	334	758	811	1.39	2.0×10^5	−5.50	−3.93	20 ± 1 (21)
IUIC2	370	806	865	1.25	2.0×10^5	−5.32	−3.86	3.9 ± 0.6 (4.7)

^{a}Average values with standard deviation were obtained from over 10 devices, and the best values are in parentheses.

Table 2. Performance of the Optimized OSC Devices Based on PTB7-Th:Acceptor

acceptor	V_{OC} (V)^a	J_{SC} (mA cm^{-2})^a	FF^a	PCE^a (%)	calcd J_{SC} (mA cm^{-2})	E_{loss} (eV)	mobility (10^{-4} cm^2 V^{-1} s^{-1})^b		μ_h/μ_e	IQE (%)
							μ_h	μ_e		
F5IC	0.641 ± 0.003	13.43 ± 0.61 (13.89)	0.621 ± 0.011 (0.630)	5.31 ± 0.23 (5.61)	13.14	1.00	4.2 ± 0.5 (4.8)	2.1 ± 0.6 (3.0)	1.6	85
AOIC	0.742 ± 0.002	24.32 ± 0.51 (24.51)	0.743 ± 0.008 (0.750)	13.3 ± 0.2 (13.7)	24.34	0.65	27 ± 1 (29)	23 ± 2 (27)	1.1	90
IUIC2	0.758 ± 0.005	10.77 ± 0.89 (11.03)	0.515 ± 0.019 (0.533)	4.06 ± 0.41 (4.48)	11.36	0.49	5.8 ± 1.0 (7.1)	0.14 ± 0.01 (0.18)	39.4	40

^{a}Average values with standard deviations were obtained from over 20 devices. The values in parentheses are the parameters of the best device.
^{b}Average values with standard deviation were obtained from over 10 devices, and the best values are in parentheses.

atures (T_d) of 334 and 370 °C, respectively, as measured by thermogravimetric analysis in nitrogen (Figure S1).

The optical absorption of solutions of F5IC, AOIC, and IUIC2 in chloroform (10^{-6} M) and in film was measured (Figures S2a and 1a). F5IC, AOIC, and IUIC2 in solution show maximum absorption peaks at 666, 758, and 806 nm, respectively, with a similar molar absorption coefficient of 2.0 × 10^5 M^{-1} cm^{-1} (Table 1). F5IC, AOIC, and IUIC2 in thin films show red-shifted absorption maxima (relative to those in solution) at 694, 811, and 865 nm, respectively. Compared to F5IC, AOIC exhibits markedly red-shifted absorption, while IUIC2 exhibits further red-shifted absorption. Estimated from the absorption edge, the optical band gaps (E_g) of F5IC, AOIC, and IUIC2 are 1.64, 1.39, and 1.25 eV, respectively. The unidirectional extension of the fused-ring core red shifts absorption and reduces E_g in a smaller step relative to the bidirectional extension.

The electrochemical properties of F5IC, AOIC, and IUIC2 were determined using cyclic voltammetry (Figure 1b). The energy levels of the lowest unoccupied molecular orbitals (LUMOs) and highest occupied molecular orbitals (HOMOs) are estimated by the onset reduction and oxidation potentials, respectively, against ferrocenium/ferrocene (FeCp$^{+/0}$). As the number of fused rings increases from F5IC to IUIC2, the HOMO up-shifts from −5.82 to −5.32 eV, and the LUMO up-

shifts from -4.05 to -3.86 eV (Figure S2b). In comparison with the bidirectional extension of the fused-ring core, the unidirectional extension modulates the energy levels of the FREAs more subtly.

Space charge limited current (SCLC)[58] was used to measure the charge mobilities of F5IC, AOIC, and IUIC2 using electron-only devices with a structure of Al/F5IC, AOIC, or IUIC2/Al in Figure S3. The medium-size AOIC shows better electron mobility (2.1×10^{-3} cm^2 V^{-1} s^{-1}) relative to that of F5IC (1.0×10^{-3} cm^2 V^{-1} s^{-1}) and IUIC2 (4.7×10^{-4} cm^2 V^{-1} s^{-1}).

Photovoltaic Properties. OSC devices with a structure of indium tin oxide (ITO)/ZnO/PFN-Br[59]/PTB7-Th:acceptor/ MoO$_x$/Ag were fabricated using PTB7-Th as the donor and F5IC, AOIC, or IUIC2 as the acceptor. Tables S1 and S2 summarize the optimization details of donor/acceptor weight ratios (D/A) and the volume contents of 1,8-diiodooctane (DIO). The optimized cells based on PTB7-Th:AOIC have an open-circuit voltage (V_{OC}) of 0.744 V, a high short-circuit current (J_{SC}) of 24.51 mA cm^{-2}, a high fill factor (FF) of 0.750, and a champion PCE of 13.7%. The optimized PTB7- Th:F5IC-based cells have a V_{OC} of 0.642 V, a J_{SC} of 13.89 mA cm^{-2}, an FF of 0.630, and a PCE of 5.61%. The optimized PTB7-Th:IUIC2-based cells have a V_{OC} of 0.762 V, a J_{SC} of 11.03 mA cm^{-2}, an FF of 0.533, and a PCE of 4.48% (Table
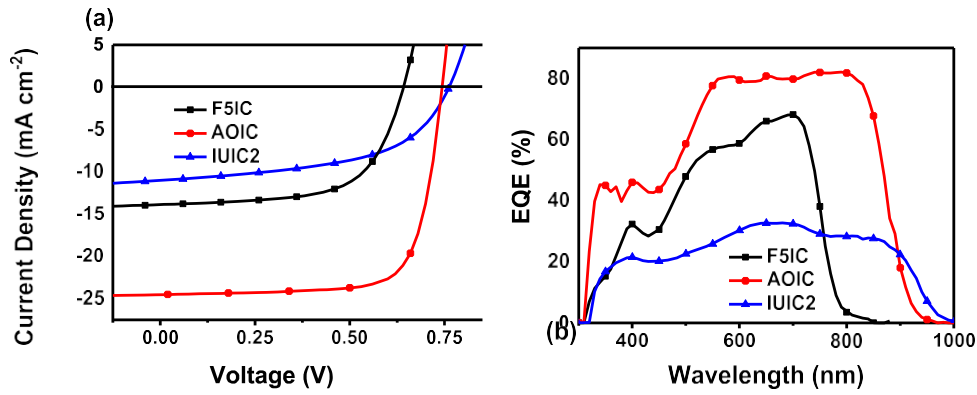
Figure 2. (a) $J-V$ curves and (b) EQE spectra of optimized devices based on PTB7-Th: F5IC, PTB7-Th:AOIC, and PTB7-Th:IUIC2.
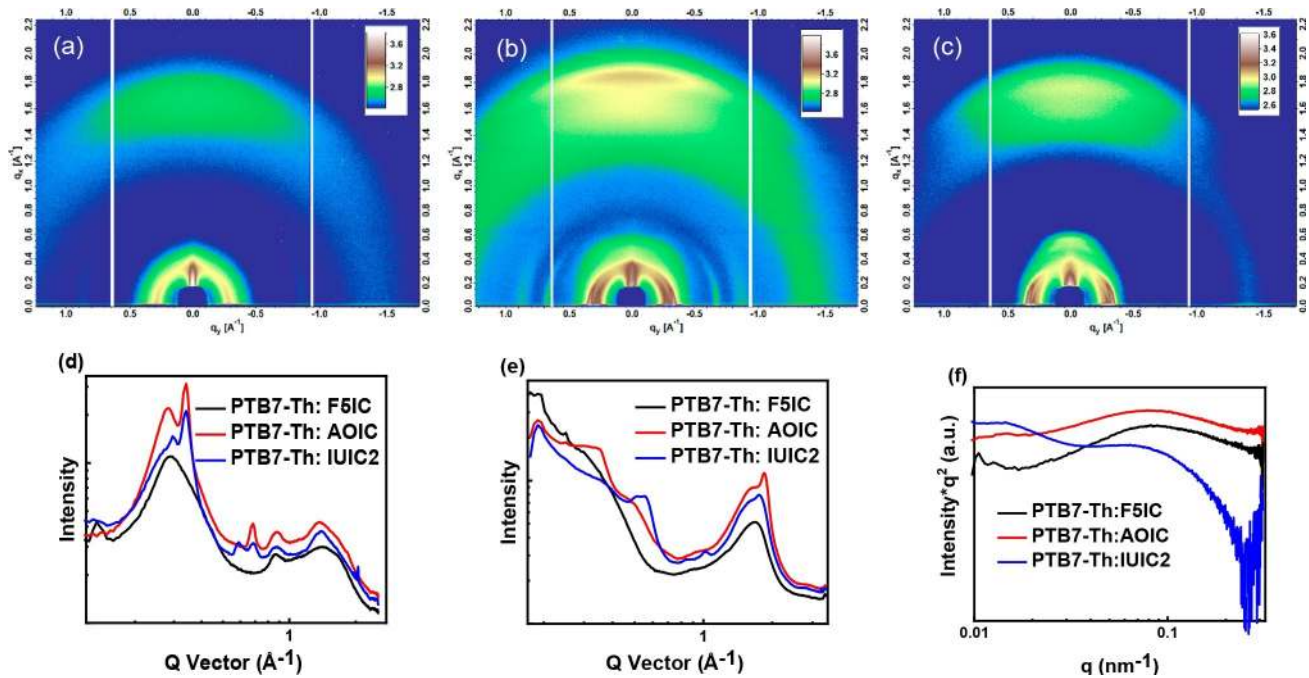

Figure 3. Two-dimensional GIWAXS diffraction images of (a) PTB7-Th:F5IC, (b) PTB7-Th:AOIC, and (c) PTB7-Th:IUIC2 blend films. GIWAXS profiles of PTB7-Th:F5IC, PTB7-Th:AOIC, and PTB7-Th:IUIC2 blend films in the (d) in-plane direction and (e) out-of-plane direction. (f) RSoXS profiles of PTB7-Th:F5IC, PTB7-Th:AOIC, and PTB7-Th:IUIC2 blend films.

2). The V_{OC} values of the OSCs increase with the extension of the fused-ring core of the acceptor, benefiting from the up- shifted LUMO level of the acceptor. The J_{SC}, FF, and PCE of AOIC-based cells are obviously higher than those of F5IC- and IUIC2-based cells.

The external quantum efficiency (EQE) of the best devices based on F5IC, AOIC, and IUIC2 shows maxima of 68% from 300 to 800 nm, 81% from 300 to 900 nm, and 32% from 300 to 950 nm, respectively (Figure 2b). The J_{SC} determined from the EQE spectra with an AM 1.5G reference spectrum is close to that measured from $J-V$ curves (Table 2).

The charge generation/extraction properties were inves- tigated by measuring the photocurrent density (J_{ph}) under different effective voltages (V_{eff}) (Figure S4a). At a high V_{eff} of

show the best charge extraction efficiency, which would benefit J_{SC} and FF.

We investigated the carrier recombination in the photoactive layers of the best devices from the relationship of V_{OC} or J_{SC} with the light intensity (P_{light}) (Figure S4b,c). The relationship of V_{OC} to P_{light} is expressed by $V_{OC} \propto \ln P_{light}$. The slopes of F5IC-, AOIC- and IUIC2-based devices are 1.22 (1.07 ± 0.12 from 10 devices) $k_B T/e$, 0.92 (0.85 ± 0.05 from 10 devices) $k_B T/e$, and 1.86 (1.68 ± 0.15 from 10 devices) $k_B T/e$ (k_B, Boltzmann constant; T, temperature; e, elementary charge). In the F5IC- and AOIC-based devices, bimolecular recombina- tion dominates, while monomolecular recombination domi- nates in the IUIC2-based devices. The relationship of J_{SC} to >2.2 V, J_{ph} approaches saturation (J_{sat}), indicating that photogenerated excitons are completely dissociated and the electrodes collect almost all

of the free charge carriers. The J_{ph}/J_{sat} values of the cells based on F5IC, AOIC, and IUIC2 are 93.1, 95.2, and 81.5%, respectively. The AOIC-based devices

P_{light} is described by $J_{SC} \propto P_{light}^{\alpha}$, where $\alpha \approx 1$ implies little carrier recombination in the cells. The α values in F5IC- and AOIC-based blend films are both 0.95 (0.94 $\pm$ 0.01 from 10 devices), which means that there is a slight bimolecular recombination, while IUIC2-based devices exhibit α of 0.88 (0.86 $\pm$ 0.02 from 10 devices), suggesting much more carrier recombination, which is responsible for lower J_{SC} and FF.
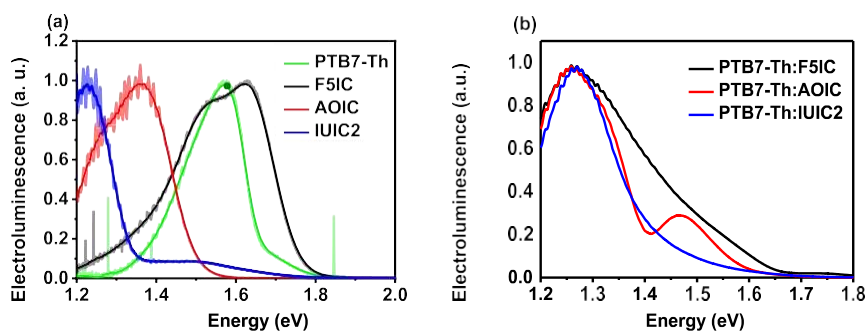
Figure 4. EL spectra of the OSCs based on (a) PTB7-Th, F5IC, AOIC, and IUIC2 and (b) PTB7-Th:F5IC, PTB7-Th:AOIC, and PTB7- Th:IUIC2 blend films.

We further employed SCLC to investigate the charge transport in the photoactive layers (Figure S5). The PTB7- Th:AOIC blend shows the highest hole mobility (μ_h) of 2.9×10^{-3} cm^2 V^{-1} s^{-1} and the highest electron mobility (μ_e) of 2.7 $\times$ 10^{-3} cm^2 V^{-1} s^{-1}, and the hole/electron charge transport is well balanced (μ_h/μ_e = 1.1), which is favorable for efficient charge extraction and suppressing the bimolecular recombina- tion, giving rise to the high J_{SC} and FF (Table 2). The PTB7-Th:IUIC2 blend shows the lowest μ_e of 1.8×10^{-5} cm^2 V^{-1} s^{-1}, and the hole/electron charge transport is unbalanced (μ_h/μ_e = 39.4), which is unfavorable for charge extraction and causes carrier recombination, giving rise to the low J_{SC} and FF. The PTB7-Th:F5IC blend shows medium μ_h and μ_e with balanced charge transport (μ_h/μ_e = 1.6), leading to medium J_{SC} and FF

Furthermore, we investigated the stability of the devices based on PTB7-Th:F5IC, PTB7-Th:AOIC, and PTB7-Th:IUIC2 blends (Figure S6). The PCEs of devices based on the three blends retained over 90% of their original values under AM 1.5G illumination at 100 mW cm^{-2} for 180 min. The PCEs of devices based on F5IC, AOIC, and IUIC2 retained 73, 63, and 54% of their original values, respectively, under heating at 100 °C for 180 min.

Film Morphology. The surface morphologies of the PTB7-Th:F5IC-, PTB7-Th:AOIC-, and PTB7-Th:IUIC2- based active layers were investigated by atomic force microscopy (AFM). From the AFM height images, the blends of PTB7-Th:F5IC and PTB7-Th:AOIC are much smoother with root-mean-square roughness (R_q) values of 2.6 and 1.5 nm, respectively, relative to that of PTB7-Th:IUIC2 (R_q ≈ 15.0 nm) (Figure S7a−c). Moreover, fibrillar structures are observed from the phase images of PTB7-Th:F5IC and PTB7- Th:AOIC films (Figure S7d−f), which is beneficial to charge transport in the OSCs.

Grazing-incidence wide-angle X-ray scattering (GIWAXS) was used to investigate the molecular orientation and packing of the neat and blended films containing PTB7-Th and different acceptors. Two-dimensional GIWAXS diffraction profiles and linear cuts of the profiles are shown in Figures 3a−e and S8. PTB7-Th shows a sharp in-plane (100) peak at 0.29 Å^{-1} and an out-of-plane (010) π−π packing peak at 1.66 Å^{-1}, reflecting the preferable face-on orientation. IUIC2 shows an intense (100) peak at 0.34 Å^{-1} and a (200) peak at 0.68 Å^{-1} in the in-plane direction as well as a strong (010) peak at 1.82 Å^{-1} in the out-of-plane direction, indicative of face-on orientation and a high degree of crystallinity. AOIC shows a (100) peak at 0.36 Å^{-1} in the in-plane direction and a (010) peak at 1.75 Å^{-1} in the out-of-plane direction. F5IC shows a

peak at 0.38 Å^{-1} in the in-plane direction and a (010) peak at 1.50 Å^{-1} in the out-of-plane direction. Both AOIC and F5IC show a lower crystallinity than IUIC2 (Table S3). F5IC is isotropic with no preferred orientation. AOIC and IUIC2 show face-on and edge-on orientations in the neat films. In the PTB7-Th:F5IC blend film, the in-plane (100) peak and the out-of-plane (010) peak of PTB7-Th remain at 0.29 and 1.66 Å^{-1}, respectively. The diffraction peaks of PTB7-Th are also seen in the diffraction profiles of the PTB7-Th:AOIC and PTB7-Th:IUIC2 blend films, while the (100) diffraction peaks of the acceptors in the in-plane direction are sharper. The out- of-plane (010) diffraction peaks of PTB7-Th:F5IC, PTB7- Th:AOIC, and PTB7-Th:IUIC2 blend films are 1.66, 1.83, and 1.75 Å^{-1}, respectively (d = 3.79, 3.43, and 3.59 Å). The smaller π−π stacking distance in the PTB7-Th:AOIC blend film is beneficial to charge transport. Thus, the fused-8-ring acceptor yields a suitable crystal size and a closer π−π stacking distance when blended with PTB7-Th, leading to the high performance of PTB7-Th:AOIC devices.

Resonant soft X-ray scattering (R-SoXS) at the carbon edge (284.2 eV) was used to assess the phase separation of PTB7- Th:F5IC, PTB7-Th:AOIC, and PTB7-Th:IUIC2 blend films. The scattering profiles are shown in Figure 3f. The domain size of the mixture can be estimated from the correlation length and the volume fractions of the components. The average domain sizes of PTB7-Th:F5IC and PTB7-Th:AOIC blend films are 40 and 39 nm, respectively. PTB7-Th:IUIC2 blend films show two peaks in the R-SoXS profiles, indicating two different domain sizes of 108 and 45 nm. The relatively larger domain size arises from the strong aggregation tendency of IUIC2. The results are consistent with the AFM phase images. All three blends have domain sizes that are appropriate for exciton dissociation.

Voltage Loss. The V_{OC} of the OSCs increases with increasing size of the fused-ring structure in the acceptor. The lowest V_{OC} is obtained from F5IC, and the highest V_{OC} is obtained from IUIC2. This is unexpected because F5IC has the largest E_g, whereas the E_g of IUIC2 is significantly smaller (Table 1). The difference in E_g is also observed in the electroluminescence (EL) spectra of the OSCs based on the pure acceptors and PTB7-Th. As shown in Figure 4a, the peak of the EL spectrum of the devices based on pure F5IC is ~1.60 eV, which is significantly blue-shifted in comparison to that of the OSCs based on AOIC (1.35 eV) or IUIC2 (1.22 eV). This suggests that F5IC has the highest E_g, whereas the E_g of IUIC2 is the smallest.

To investigate the origins of the different V_{OC}'s in the OSCs based on different acceptors, we also measured the EL of the

OSCs with blend active layers, which is expected to be red-shifted, in comparison to the EL spectra of the OSCs based on the pure donor or acceptor materials. This is because the charge transfer (CT) emission, related to the electronic structure at the D/A interface, is often dominant in the EL of bulk-heterojunction OSCs, and the CT emission energy is normally lower than that of the pure phase emission.[60,61] Indeed, the peaks of the EL spectra are at the same position for all of the OSCs based on different acceptors (Figure 4b), suggesting a similar energy of the CT state (E_{CT}) for all of the OSCs. Therefore, we conclude that the CT state is not the reason for the different V_{OC}.

Because E_{CT}'s of the OSCs are similar, the difference in V_{OC} of the OSCs must arise from the different degrees of charge carrier recombination losses. Using the detailed balance theory (Supporting Information), the total losses due to charge carrier recombination are calculated to be 0.58, 0.48, and 0.46 eV for the F5IC-, AOIC-, and IUIC2-based OSCs, respectively. The total loss due to charge carrier recombination consists of radiative recombination losses and nonradiative recombination losses. The nonradiative recombination losses are related to the electroluminescence quantum efficiency (EQE_{EL}).[62] There- fore, to assess the origin of the different recombination losses, the EQE_{EL} of the OSCs based on the different acceptors were measured using low injection currents.

As shown in Figure S9a, EQE_{EL} of the OSC based on F5IC is the lowest, with a nonradiative recombination loss value close to 0.37 eV (Figure S9b), while for the OSCs based on AOIC and IUIC2 the nonradiative recombination loss terms are slightly less than 0.3 eV. Therefore, the EQE_{EL} measure- ments confirm that the V_{OC} of the OSC based on F5IC is significantly limited by nonradiative recombination losses of charge carriers. From the EQE_{EL}, we can also see that nonradiative recombination losses at a lower injection current (relevant to V_{OC} analysis because at V_{OC} the device current is zero) are smaller in the OSC based on IUIC2, in comparison to that in the AOIC-based OSC. Therefore, the V_{OC} of the OSC based on IUIC2 is the highest. Hence, we conclude that for the OSCs based on the FREAs, E_{CT} does not depend on the fused-ring core size, but recombination losses, especially nonradiative recombination losses of charge carriers, decrease with increasing number of fused rings of the acceptor molecule, leading to a reduced energy loss (E_{loss}) and an increased V_{OC} (Table 2).

Quantum Efficiency. To determine how the increasing

number of fused rings in the acceptor molecule influences the J_{SC} of the OSC, we first measured the dielectric functions of the BHJ active layers based on the different acceptors (Figure S10). The extinction coefficients of the active layers are clearly different. The F5IC-based BHJ has the strongest but narrowest absorption, and the IUIC2-based BHJ has the weakest but broadest absorption. Because J_{SC} is determined by both the absorption strength and the spectral coverage, it is difficult to determine whether the difference in J_{SC} of the OSCs based on the different acceptors is a result of different active layer absorption strengths or is related to the degree of quantum efficiency losses. Therefore, transfer matrix modeling (TMM) was performed,[63] using the dielectric functions of the materials used in the OSC stack, to simulate the maximum achievable J_{SC} for the OSCs based on the different acceptors with different active layer thicknesses. The TMM results suggest that, in comparison to the J_{SC} of the AOIC-based solar cell, the lower experimental J_{SC} obtained from the OSC based on F5IC can be

ascribed to less photon absorption due to the narrower absorption spectrum of the active layer (Figure S11). However, the lower J_{SC} of the IUIC2-based OSC, in comparison to that of the other two OSCs, does not arise from the active layer absorption. In fact, because of the broader absorption, OSCs based on IUIC2 are expected to have the highest J_{SC}, at optimized active layer thicknesses (150 nm). Therefore, the difference between the J_{SC}'s for the OSCs based on AOIC and IUIC2 must arise from the different internal quantum efficiencies (IQEs).

In this work, IQE was calculated by taking the ratio between the measured EQE and the TMM simulated active layer absorption.[63] For the OSC based on F5IC, IQE of 85% is high (Table 2), while IQE of the OSC based on AOIC is even higher (90%). However, for the OSC based on IUIC2, IQE is only 40%, which severely limits the J_{SC} of the IUIC2-based OSC.

To investigate the origin of the different IQEs, photo-luminescence quenching measurements were performed using the different acceptors (Figure 5).[61] For the OSCs based on

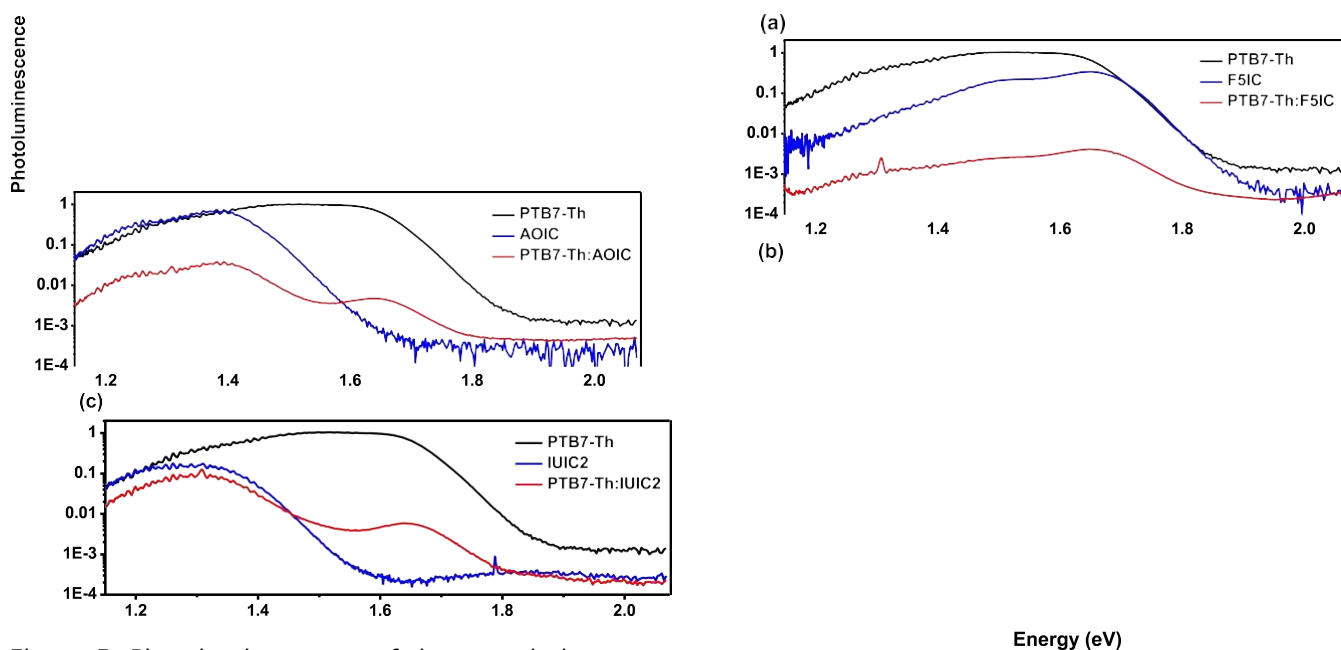dissociation efficiency depends on the degree of D/A

Figure 5. Photoluminescence of the organic layers based on (a) PTB7-Th, F5IC, and PTB7-Th:F5IC, (b) PTB7-Th, AOIC, and PTB7-Th:AOIC, and (c) PTB7-Th, IUIC2, and PTB7-Th:IUIC2.

F5IC and AOIC, the acceptor emission is high in the pure films but significantly suppressed in the BHJ active layers (Figure S12). However, for the OSC based on IUIC2, the acceptor emission from the BHJ active layer is comparable to that of the pure IUIC2 film. This suggests that excitons in the BHJ active layer based on IUIC2 are difficult to dissociate and therefore will minimally contribute to photocurrent generation, thus limiting J_{SC}.

We also performed time-resolved transient photolumines- cence (TRTPL) and observed no difference in the fluorescence lifetimes of the excitons in the active layers based on the different acceptors (Figure S13). The exciton

intermixing, exciton lifetime, and electronic structure of the D/ A interface. Because the difference in the degree of D/A intermixing is not significant and the exciton lifetime is similar, the significant differences between the exciton dissociation efficiencies of the OSCs based on F5IC, AOIC, and IUIC2 are more than likely related to the differences in the electronic structure of the D/A interface. The similar ELs obtained from the BHJ and the pure IUIC2 suggest that the energetic driving force for an exciton to dissociate is very small, which can thus limit the exciton dissociation efficiency and J_{SC} of the OSC based on IUIC2. The small driving force for exciton splitting is caused by improper energy levels of IUIC2 which are not well aligned with those of PTB7-Th. These results prove that precise modulation of the electronic properties of the acceptors is essential for device performance and the unidirectional extension strategy is more effective than the bidirectional extension in terms of fine molecular structure tailoring and the property modulation of organic materials.

Furthermore, we investigated the general applicability of
AOIC with often-used polymer donors, such as medium-band- gap donors PM6[64] (E_g = 1.80 eV) and PM7[65] (E_g = 1.79 eV) and wide-band-gap donor J71[66] (E_g = 1.96 eV) (Table S4). The champion cells based on these polymers yield PCEs of
>10%, demonstrating the good suitability of AOIC for typical polymer donors with a broad scope from a wide band gap to medium and low band gaps.

CONCLUSIONS

We designed and synthesized a unidirectionally extended FREA, AOIC, and its bidirectionally extended counterpart IUIC2 by the nontoxic Negishi cross coupling reaction and compared these with their parent molecule F5IC. F5IC, AOIC, and IUIC2 share the same electron-deficient terminal groups, 2FIC, and the same side substituent, 4-hexylphenyl, but have different fused-ring electron-rich cores. From the fused-5-ring F5IC to the fused-11-ring IUIC2, elevated energy levels, red- shifted absorption, and narrowed band gaps are observed. The
OSCs based on AOIC with a fused-8-ring core yield the best PCE of ~13.7%, while the OSCs based on F5IC with a fused- 5-ring core and IUIC2 with a fused-11-ring core have much lower PCEs of 5.61 and 4.48%, respectively. From the EL spectra of OSCs based on the different acceptors, we found
that recombination losses, especially nonradiative recombina- tion losses of charge carriers, are reduced with an increasing number of fused rings in the acceptor molecule, accounting for the observed differences in the V_{OC}'s of the OSCs. Furthermore, as the number of fused rings in the acceptor molecule increases, the

absorption spectrum broadens, enhancing the J_{SC}. However, the driving force for exciton dissociation in the IUIC2-based OSC is too small, limiting the

Experimental details and additional characterization, such as TGA, absorption spectra in solution, energy levels, SCLC, AFM, GIWAXS, EQE EL, TMM, TRTPL, ^{1}H and ^{13}C NMR spectra, and the optimization of the OSC devices (PDF)

AUTHOR INFORMATION

Corresponding Author
*E-mail: xwzhan@pku.edu.cn.
ORCID
Yao Wu: 0000-0002-6680-7347
Zheng Tang: 0000-0003-0036-2362
Thomas P. Russell: 0000-0001-6384-5826
Xiaowei Zhan: 0000-0002-1006-3342
Notes
The authors declare no competing financial interest.

J_{SC}. As a result, AOIC performs best among these three FREAs. These results show that unidirectionally extending the fused- ring core has advantages over bidirectional extension to finely tailor molecular structure and therefore precisely modulate the electronic properties of FREAs, allowing for efficient optimization of the device performance of OSCs. This unidirectional extension strategy may open up avenues to other organic materials with wide applicability.

REFERENCES

(1) Cheng, Y. J.; Yang, S. H.; Hsu, C. S. Synthesis of conjugated polymers for organic solar cell applications. *Chem. Rev.* 2009, *109*, 5868−5923.
(2) Lu, L.; Zheng, T.; Wu, Q.; Schneider, A. M.; Zhao, D.; Yu, L. Recent Advances in Bulk Heterojunction Polymer Solar Cells. *Chem. Rev.* 2015, *115*, 12666−12731.
(3) Li, G.; Zhu, R.; Yang, Y. Polymer solar cells. *Nat. Photonics* 2012, *6*, 153−161.
(4) Lin, Y.; Li, Y.; Zhan, X. Small molecule semiconductors for high- efficiency organic photovoltaics. *Chem. Soc. Rev.* 2012, *41*, 4245−4272.
(5) Lin, Y.; Zhan, X. Non-fullerene acceptors for organic photovoltaics: an emerging horizon. *Mater. Horiz.* 2014, *1*, 470−488.
(6) Anthony, J. E.; Facchetti, A.; Heeney, M.; Marder, S. R.; Zhan, X. n-Type Organic Semiconductors in Organic Electronics. *Adv. Mater.* 2010, *22*, 3876−3892.
(7) Yan, C.; Barlow, S.; Wang, Z.; Yan, H.; Jen, A. K. Y.; Marder, S. R.; Zhan, X. Non-fullerene acceptors for organic solar cells. *Nat. Rev. Mater.* 2018, *3*, 18003.
(8) Cheng, P.; Li, G.; Zhan, X.; Yang, Y. Next-generation organic photovoltaics based on non-fullerene acceptors. *Nat. Photonics* 2018, *12*, 131−142.
(9) Hou, J.; Inganas, O.; Friend, R. H.; Gao, F. Organic solar cells based on non-fullerene acceptors. *Nat. Mater.* 2018, *17*, 119−128.
(10) Zhan, X.; Tan, Z.; Domercq, B.; An, Z.; Zhang, X.; Barlow, S.; Li, Y.; Zhu, D.; Kippelen, B.; Marder, S. R. A high-mobility electron- transport polymer with broad absorption and its use in field-effect transistors and all-polymer solar cells. *J. Am. Chem. Soc.* 2007, *129*, 7246−7247.
(11) Li, H.; Earmme, T.; Ren, G.; Saeki, A.; Yoshikawa, S.; Murari, N. M.; Subramaniyan, S.; Crane, M. J.; Seki, S.; Jenekhe, S. A. Beyond fullerenes: design of nonfullerene acceptors for efficient organic photovoltaics. *J. Am. Chem. Soc.* 2014, *136*, 14589−14597.
(12) Zhong, Y.; Trinh, M. T.; Chen, R. S.; Purdum, G. E.; Khlyabich, P. P.; Sezen, M.; Oh, S.; Zhu, H.; Fowler, B.; Zhang, B.; Wang, W.; Nam, C. Y.; Sfeir, M. Y.; Black, C. T.; Steigerwald, M. L.;

Loo, Y. L.; Ng, F.; Zhu, X. Y.; Nuckolls, C. Molecular helices as electron acceptors in high-performance bulk heterojunction solar cells. *Nat. Commun.* 2015, *6*, 8242.

(13) Meng, D.; Sun, D.; Zhong, C.; Liu, T.; Fan, B.; Huo, L.; Li, Y.; Jiang, W.; Choi, H.; Kim, T.; Kim, J. Y.; Sun, Y.; Wang, Z.; Heeger, A.
J. High-Performance Solution-Processed Non-Fullerene Organic Solar Cells Based on Selenophene-Containing Perylene Bisimide Acceptor. *J. Am. Chem. Soc.* 2016, *138*, 375−380.

(14) Wu, Q.; Zhao, D.; Schneider, A. M.; Chen, W.; Yu, L.
Covalently Bound Clusters of Alpha-Substituted PDI-Rival Electron Acceptors to Fullerene for Organic Solar Cells. *J. Am. Chem. Soc.* 2016, *138*, 7248−7251.

(15) Liu, J.; Chen, S.; Qian, D.; Gautam, B.; Yang, G.; Zhao, J.;
Bergqvist, J.; Zhang, F.; Ma, W.; Ade, H.; Inganaš, O.; Gundogdu, K.; Gao, F.; Yan, H. Fast charge separation in a non-fullerene organic solar cell with a small driving force. *Nat. Energy* 2016, *1*, 16089.

(16) Zhang, J.; Li, Y.; Huang, J.; Hu, H.; Zhang, G.; Ma, T.; Chow,
P. C. Y.; Ade, H.; Pan, D.; Yan, H. Ring-Fusion of Perylene Diimide Acceptor Enabling Efficient Nonfullerene Organic Solar Cells with a Small Voltage Loss. *J. Am. Chem. Soc.* 2017, *139*, 16092−16095.

(17) Liu, X.; Du, X.; Wang, J.; Duan, C.; Tang, X.; Heumueller, T.;
Liu, G.; Li, Y.; Wang, Z.; Wang, J.; Liu, F.; Li, N.; Brabec, C. J.; Huang, F.; Cao, Y. Efficient Organic Solar Cells with Extremely High Open-Circuit Voltages and Low Voltage Losses by Suppressing Nonradiative Recombination Losses. *Adv. Energy Mater.* 2018, *8*, 1801699.

(18) Lin, Y.; Wang, J.; Zhang, Z. G.; Bai, H.; Li, Y.; Zhu, D.; Zhan,
X. An electron acceptor challenging fullerenes for efficient polymer solar cells. *Adv. Mater.* 2015, *27*, 1170−1174.

(19) Xiao, Z.; Jia, X.; Ding, L. Ternary organic solar cells offer 14% power conversion efficiency. *Sci. Bull.* 2017, *62*, 1562−1564.

(20) Lin, Y.; Zhao, F.; Prasad, S. K. K.; Chen, J. D.; Cai, W.; Zhang,
Q. ; Chen, K.; Wu, Y.; Ma, W.; Gao, F.; Tang, J. X.; Wang, C.; You,
W. ; Hodgkiss, J. M.; Zhan, X. Balanced Partnership between Donor and Acceptor Components in Nonfullerene Organic Solar Cells with > 12% Efficiency. *Adv. Mater.* 2018, *30*, 1706363.

(21) Cheng, P.; Liu, Y.; Chang, S.-Y.; Li, T.; Sun, P.; Wang, R.; Cheng, H.-W.; Huang, T.; Meng, L.; Nuryyeva, S.; Zhu, C.; Wei, K.- H.; Sun, B.; Zhan, X.; Yang, Y. Efficient Tandem Organic
Photovoltaics with Tunable Rear Sub-cells. *Joule* 2019, *3*, 432−442.

(22) Chandrabose, S.; Chen, K.; Barker, A. J.; Sutton, J. J.; Prasad, S.
K. K.; Zhu, J.; Zhou, J.; Gordon, K. C.; Xie, Z.; Zhan, X.; Hodgkiss, J.
M. High Exciton Diffusion Coefficients in Fused Ring Electron Acceptor Films. *J. Am. Chem. Soc.* 2019, *141*, 6922−6929.

(23) Zheng, Z.; Hu, Q.; Zhang, S.; Zhang, D.; Wang, J.; Xie, S.;
Wang, R.; Qin, Y.; Li, W.; Hong, L.; Liang, N.; Liu, F.; Zhang, Y.; Wei, Z.; Tang, Z.; Russell, T. P.; Hou, J.; Zhou, H. A Highly Efficient Non-Fullerene Organic Solar Cell with a Fill Factor over 0.80 Enabled by a Fine-Tuned Hole-Transporting Layer. *Adv. Mater.*
2018, *30*, 1801801.

(24) Yuan, J.; Zhang, Y.; Zhou, L.; Zhang, G.; Yip, H.-L.; Lau, T.-K.; Lu, X.; Zhu, C.; Peng, H.; Johnson, P. A.; Leclerc, M.; Cao, Y.; Ulanski, J.; Li, Y.; Zou, Y. Single-Junction Organic Solar Cell with over 15% Efficiency Using Fused-Ring Acceptor with Electron-
Deficient Core. *Joule* 2019, *3*, 1140−1151.

(25) Cui, Y.; Yao, H.; Hong, L.; Zhang, T.; Xu, Y.; Xian, K.; Gao, B.;
Qin, J.; Zhang, J.; Zhixiang, Wei; Hou, J. Achieving Over 15% Efficiency in Organic Photovoltaic Cells via Copolymer Design. *Adv. Mater.* 2019, *31*, 1808356.

(26) Fan, B.; Zhang, D.; Li, M.; Zhong, W.; Zeng, Z.; Ying, L.; Huang, F.; Cao, Y. Achieving over 16% efficiency for single-junction organic solar cells. *Sci. China: Chem.* 2019, *62*, 746−752.

(27) Meng, L.; Zhang, Y.; Wan, X.; Li, C.; Zhang, X.; Wang, Y.; Ke,
X. ; Xiao, Z.; Ding, L.; Xia, R.; Yip, H. L.; Cao, Y.; Chen, Y. Organic and solution-processed tandem solar cells with 17.3% efficiency. *Science* 2018, *361*, 1094−1098.

(28) Wang, J.; Zhang, J.; Xiao, Y.; Xiao, T.; Zhu, R.; Yan, C.; Fu, Y.;
Lu, G.; Lu, X.; Marder, S. R.; Zhan, X. Effect of Isomerization on

High-Performance Nonfullerene Electron Acceptors. *J. Am. Chem. Soc.*
2018, *140*, 9140−9147.

(29) Li, T.; Dai, S.; Ke, Z.; Yang, L.; Wang, J.; Yan, C.; Ma, W.;
Zhan, X. Fused Tris(thienothiophene)-Based Electron Acceptor with Strong Near-Infrared Absorption for High-Performance As-Cast Solar Cells. *Adv. Mater.* 2018, *30*, 1705969.

(30) Zhu, J.; Ke, Z.; Zhang, Q.; Wang, J.; Dai, S.; Wu, Y.; Xu, Y.; Lin, Y.; Ma, W.; You, W.; Zhan, X. Naphthodithiophene-Based Non- fullerene Acceptor for High-Performance Organic Photovoltaics: Effect of Extended Conjugation. *Adv. Mater.* 2018, *30*, 1704713.

(31) Wang, W.; Yan, C.; Lau, T. K.; Wang, J.; Liu, K.; Fan, Y.; Lu, X.; Zhan, X. Fused Hexacyclic Nonfullerene Acceptor with Strong Near-Infrared Absorption for Semitransparent Organic Solar Cells with 9.77% Efficiency. *Adv. Mater.* 2017, *29*, 1701308.

(32) Dai, S.; Li, T.; Wang, W.; Xiao, Y.; Lau, T. K.; Li, Z.; Liu, K.; Lu, X.; Zhan, X. Enhancing the Performance of Polymer Solar Cells via Core Engineering of NIR-Absorbing Electron Acceptors. *Adv. Mater.* 2018, *30*, 1706571.

(33) Liu, W.; Zhang, J.; Zhou, Z.; Zhang, D.; Zhang, Y.; Xu, S.; Zhu,
X. Design of a New Fused-Ring Electron Acceptor with Excellent Compatibility to Wide-Bandgap Polymer Donors for High-Perform- ance Organic Photovoltaics. *Adv. Mater.* 2018, *30*, 1800403.

(34) Kan, B.; Feng, H.; Wan, X.; Liu, F.; Ke, X.; Wang, Y.; Wang, Y.; Zhang, H.; Li, C.; Hou, J.; Chen, Y. Small-Molecule Acceptor Based on the Heptacyclic Benzodi(cyclopentadithiophene) Unit for Highly Efficient Nonfullerene Organic Solar Cells. *J. Am. Chem. Soc.* 2017, *139*, 4929−4934.

(35) Qiu, N.; Zhang, H.; Wan, X.; Li, C.; Ke, X.; Feng, H.; Kan, B.;
Zhang, H.; Zhang, Q.; Lu, Y.; Chen, Y. A New Nonfullerene Electron Acceptor with a Ladder Type Backbone for High-Performance Organic Solar Cells. *Adv. Mater.* 2017, *29*, 1604964.

(36) Dai, S.; Zhao, F.; Zhang, Q.; Lau, T. K.; Li, T.; Liu, K.; Ling, Q.; Wang, C.; Lu, X.; You, W.; Zhan, X. Fused Nonacyclic Electron Acceptors for Efficient Polymer Solar Cells. *J. Am. Chem. Soc.* 2017, *139*, 1336−1343.

(37) Lin, Y.; Zhao, F.; He, Q.; Huo, L.; Wu, Y.; Parker, T. C.; Ma,
W.; Sun, Y.; Wang, C.; Zhu, D.; Heeger, A. J.; Marder, S. R.; Zhan, X. High-Performance Electron Acceptor with Thienyl Side Chains for Organic Photovoltaics. *J. Am. Chem. Soc.* 2016, *138*, 4955−4961.

(38) Zhao, F.; Dai, S.; Wu, Y.; Zhang, Q.; Wang, J.; Jiang, L.; Ling,
Q.; Wei, Z.; Ma, W.; You, W.; Wang, C.; Zhan, X. Single-Junction Binary-Blend Nonfullerene Polymer Solar Cells with 12.1% Efficiency. *Adv. Mater.* 2017, *29*, 1700144.

(39) Zhao, W.; Li, S.; Yao, H.; Zhang, S.; Zhang, Y.; Yang, B.; Hou,
J. Molecular Optimization Enables over 13% Efficiency in Organic Solar Cells. *J. Am. Chem. Soc.* 2017, *139*, 7148−7151.

(40) Li, S.; Ye, L.; Zhao, W.; Liu, X.; Zhu, J.; Ade, H.; Hou, J. Design
of a New Small-Molecule Electron Acceptor Enables Efficient Polymer Solar Cells with High Fill Factor.

Adv. Mater. 2017, *29*, 1704051.

(41) Li, S.; Ye, L.; Zhao, W.; Zhang, S.; Mukherjee, S.; Ade, H.; Hou, J. Energy-Level Modulation of Small-Molecule Electron Acceptors to Achieve over 12% Efficiency in Polymer Solar Cells.
Adv. Mater. 2016, *28*, 9423−9429.

(42) Luo, Z.; Bin, H.; Liu, T.; Zhang, Z. G.; Yang, Y.; Zhong, C.;
Qiu, B.; Li, G.; Gao, W.; Xie, D.; Wu, K.; Sun, Y.; Liu, F.; Li, Y.; Yang,
C. Fine-Tuning of Molecular Packing and Energy Level through Methyl Substitution Enabling Excellent Small Molecule Acceptors for Nonfullerene Polymer Solar Cells with Efficiency up to 12.54. *Adv. Mater.* 2018, *30*, 1706124.

(43) Baran, D.; Ashraf, R. S.; Hanifi, D. A.; Abdelsamie, M.; Gasparini, N.; Rohr, J. A.; Holliday, S.; Wadsworth, A.; Lockett, S.; Neophytou, M.; Emmott, C. J.; Nelson, J.; Brabec, C. J.; Amassian, A.; Salleo, A.; Kirchartz, T.; Durrant, J. R.; McCulloch, I. Reducing the efficiency-stability-cost gap of organic photovoltaics with highly efficient and stable small molecule acceptor ternary solar cells. *Nat. Mater.* 2017, *16*, 363−369.

(44) Wu, Y.; Bai, H.; Wang, Z.; Cheng, P.; Zhu, S.; Wang, Y.; Ma, W.; Zhan, X. A planar electron acceptor for efficient polymer solar cells. *Energy Environ. Sci.* 2015, *8*, 3215−3221.

(45) Lin, Y.; He, Q.; Zhao, F.; Huo, L.; Mai, J.; Lu, X.; Su, C. J.; Li, T.; Wang, J.; Zhu, J.; Sun, Y.; Wang, C.; Zhan, X. A Facile Planar Fused-Ring Electron Acceptor for As-Cast Polymer Solar Cells with 8.71% Efficiency. *J. Am. Chem. Soc.* 2016, *138*, 2973−2976.

(46) Yang, Y.; Zhang, Z. G.; Bin, H.; Chen, S.; Gao, L.; Xue, L.; Yang, C.; Li, Y. Side-Chain Isomerization on an n-type Organic Semiconductor ITIC Acceptor Makes 11.77% High Efficiency Polymer Solar Cells. *J. Am. Chem. Soc.* 2016, *138*, 15011−15018.

(47) Aldrich, T. J.; Matta, M.; Zhu, W.; Swick, S. M.; Stern, C. L.; Schatz, G. C.; Facchetti, A.; Melkonyan, F. S.; Marks, T. J. Fluorination Effects on Indacenodithienothiophene Acceptor Packing and Electronic Structure, End-Group Redistribution, and Solar Cell Photovoltaic Response. *J. Am. Chem. Soc.* 2019, *141*, 3274−3287.

(48) Liu, Y.; Zhang, Z.; Feng, S.; Li, M.; Wu, L.; Hou, R.; Xu, X.; Chen, X.; Bo, Z. Exploiting Noncovalently Conformational Locking as a Design Strategy for High Performance Fused-Ring Electron Acceptor Used in Polymer Solar Cells. *J. Am. Chem. Soc.* 2017, *139*, 3356−3359.

(49) Li, Y.; Lin, J. D.; Che, X.; Qu, Y.; Liu, F.; Liao, L. S.; Forrest, S. R. High Efficiency Near-Infrared and Semitransparent Non-Fullerene Acceptor Organic Photovoltaic Cells. *J. Am. Chem. Soc.* 2017, *139*, 17114−17119.

(50) Yao, Z.; Liao, X.; Gao, K.; Lin, F.; Xu, X.; Shi, X.; Zuo, L.; Liu, F.; Chen, Y.; Jen, A. K. Dithienopicenocarbazole-Based Acceptors for Efficient Organic Solar Cells with Optoelectronic Response Over 1000 nm and an Extremely Low Energy Loss. *J. Am. Chem. Soc.* 2018, *140*, 2054−2057.

(51) Xiao, Z.; Yang, S.; Yang, Z.; Yang, J.; Yip, H. L.; Zhang, F.; He, F.; Wang, T.; Wang, J.; Yuan, Y.; Yang, H.; Wang, M.; Ding, L. Carbon-Oxygen-Bridged Ladder-Type Building Blocks for Highly Efficient Nonfullerene Acceptors. *Adv. Mater.* 2019, *31*, 1804790.

(52) Dai, S.; Xiao, Y.; Xue, P.; James Rech, J.; Liu, K.; Li, Z.; Lu, X.; You, W.; Zhan, X. Effect of Core Size on Performance of Fused-Ring Electron Acceptors. *Chem. Mater.* 2018, *30*, 5390−5396.

(53) Gao, W.; Zhang, M.; Liu, T.; Ming, R.; An, Q.; Wu, K.; Xie, D.; Luo, Z.; Zhong, C.; Liu, F.; Zhang, F.; Yan, H.; Yang, C. Asymmetrical Ladder-Type Donor-Induced Polar Small Molecule Acceptor to Promote Fill Factors Approaching 77% for High-Performance Nonfullerene Polymer Solar Cells. *Adv. Mater.* 2018, *30*, 1800052.

(54) Sun, J.; Ma, X.; Zhang, Z.; Yu, J.; Zhou, J.; Yin, X.; Yang, L.; Geng, R.; Zhu, R.; Zhang, F.; Tang, W. Dithieno[3,2-b:2′,3′-d]pyrrol Fused Nonfullerene Acceptors Enabling Over 13% Efficiency for Organic Solar Cells. *Adv. Mater.* 2018, *30*, 1707150.

(55) Jia, B.; Dai, S.; Ke, Z.; Yan, C.; Ma, W.; Zhan, X. Breaking 10% Efficiency in Semitransparent Solar Cells with Fused-Undecacyclic Electron Acceptor. *Chem. Mater.* 2018, *30*, 239−245.

(56) Knupfer, M. Exciton binding energies in organic semi- conductors. *Appl. Phys. A: Mater. Sci. Process.* 2003, *77*, 623−626.

(57) Liao, S. H.; Jhuo, H. J.; Cheng, Y. S.; Chen, S. A. Fullerene Derivative-Doped Zinc Oxide Nanofilm as the Cathode of Inverted Polymer Solar Cells with Low-Bandgap Polymer (PTB7-Th) for High Performance. *Adv. Mater.* 2013, *25*, 4766−4771.

(58) Malliaras, G. G.; Salem, J. R.; Brock, P. J.; Scott, C. Electrical characteristics and efficiency of single-layer organic light-emitting diodes. *Phys. Rev. B: Condens. Matter Mater. Phys.* 1998, *58*, R13411.

(59) Huang, F.; Wu, H. B.; Wang, D.; Yang, W.; Cao, Y. Novel electroluminescent conjugated polyelectrolytes based on polyfluorene. *Chem. Mater.* 2004, *16*, 708−716.

(60) Tvingstedt, K.; Vandewal, K.; Gadisa, A.; Zhang, F.; Manca, J.; Inganaš, O. Electroluminescence from charge transfer states in polymer solar cells. *J. Am. Chem. Soc.* 2009, *131*, 11819−11824.

(61) Tvingstedt, K.; Vandewal, K.; Zhang, F. L.; Inganaš, O. On the Dissociation Efficiency of Charge Transfer Excitons and Frenkel Excitons in Organic Solar Cells: A Luminescence Quenching Study. *J. Phys. Chem. C* 2010, *114*, 21824−21832.

(62) Vandewal, K.; Tvingstedt, K.; Gadisa, A.; Inganaš, O.; Manca, J.
V. Relating the open-circuit voltage to interface molecular properties of donor:acceptor bulk heterojunction solar cells. *Phys. Rev. B: Condens. Matter Mater. Phys.* 2010, *81*, 125204.

(63) Pettersson, L. A. A.; Roman, L. S.; Inganaš, O. Modeling
photocurrent action spectra of photovoltaic devices based on organic thin films. *J. Appl. Phys.* 1999, *86*, 487−496.

(64) Zhang, M.; Guo, X.; Ma, W.; Ade, H.; Hou, J. A Large-Bandgap
Conjugated Polymer for Versatile Photovoltaic Applications with High Performance. *Adv. Mater.* 2015, *27*, 4655−4660.

(65) Fan, Q.; Zhu, Q.; Xu, Z.; Su, W.; Chen, J.; Wu, J.; Guo, X.; Ma,
W. ; Zhang, M.; Li, Y. Chlorine substituted 2D-conjugated polymer for high-performance polymer solar cells with 13.1% efficiency via toluene processing. *Nano Energy* 2018, *48*, 413−420.

(66) Bin, H.; Gao, L.; Zhang, Z. G.; Yang, Y.; Zhang, Y.; Zhang, C.;
Chen, S.; Xue, L.; Yang, C.; Xiao, M.; Li, Y. 11.4% Efficiency non- fullerene polymer solar cells with trialkylsilyl substituted 2D- conjugated polymer as donor. *Nat. Commun.* 2016, *7*, 13651.